Nonreciprocity of Gigahertz Surface Acoustic Wave Based on Mode Conversion in an Inclined Phononic Crystal Heterojunction

Rahman Sharaf,[1] Sara Darbari,[1,*] and Abdelkrim Khelif[2]

[1] *Nano Sensors and Detectors Laboratory, Nano Plasmophotonic Research Group, Faculty of Electrical and Computer Engineering, Tarbiat Modares University, Tehran 1411713116, Iran*

[2] *FEMTO-ST Institute, UBFC, CNRS, ENSMM, UTBM, 15B Avenue des Montboucons, 25030 Besançon, France*

(Received 15 June 2021; revised 29 August 2021; accepted 8 October 2021; published 2 November 2021)

In this report, a rectifying surface acoustic wave (SAW) device is proposed and simulated based on a simple inclined phononic crystal (PnC) heterojunction, consisting of monolithic pillars on Si substrate. The designed nonreciprocal operation principle is initially based on the frequency alignment of the surface-coupled guiding bands in the first half of the PnC with the local-surface-resonance (LSR) band gap in the second half of the PnC, along two different equivalent incident directions. Benefiting from flexible LSR band-gap engineering, we tune the band-gap central frequency by optimizing the structural dimensions of the pillars in a small chip area, which is not achievable in conventional Bragg band gaps without varying the lattice constant. The other physical principle that dominantly affects the broken reciprocity in our proposed structure is the induced SAW shear-to-sagittal mode conversion at a limited frequency range in the trapezoidal PnC half, which depends on the incident direction with respect to the inclined cut line of the PnC. Moreover, we optimize the spacing gap between the PnCs to modulate the elastic coupling strength between the half PnCs, and prove a significant SAW nonreciprocity of 34 dB at a frequency of 6.9 GHz, in addition to an acceptable rectified transmission of about −10.68 dB, by the proposed PnC-based operation principles. The presented design benefits from a simple Si-based structure and a CMOS-compatible fabrication process, without the need for any external excitation, and it is a promising miniature and efficient SAW rectifying candidate for wireless-communication applications.

DOI: 10.1103/PhysRevApplied.16.054004

I. INTRODUCTION

Nonreciprocity is defined as breaking symmetry in the forward and backward transmissions of a system in response to different incident wave directions [1]. Rectifiers, isolators, and circulators are different types of nonreciprocal devices that have found many applications in electromagnetics, acoustics, and elastic fields [2–5]. There is much interest in nonreciprocal structures at microwave frequencies beyond 100 MHz for controlling wave propagation in radio-frequency communications, quantum-technology systems, and on-chip-processing applications [6–9]. However, realizing both magnetic free nonreciprocal behavior and CMOS-compatible fabrication technology remain challenging and desirable issues [6].

Surface acoustic wave (SAW) devices have the potential to use elastic waves instead of electromagnetic waves in radar receivers to replace bulky devices (mm–m) with micrometer SAW counterparts, because of the lower speed of elastic phonons than that of a photon [10]. SAW devices are attractive for a wide range of applications [11], such as on-chip RF filters, an impartible component in wireless communications [12], microfluidics [13], different kinds of sensors [14,15], hybrid quantum technologies [16], and acousto-optic and acoustoelectric devices [17–19]. Benefiting from SAW devices, elastic nonreciprocity is practical for frequency ranges from a few hundreds of MHz to several GHz, wherein low-loss devices with micrometer and submicrometer dimensions are feasible [20]. Some recent reports on elastic nonreciprocity use external excitations to change the material-elastic wave coupling in the delay line through magnetoelastic and acoustoelectric effects [5,7,20,21]. However, these material-based reports on SAW nonreciprocity involve incompatibility challenges in fabricating and scaling down the proposed nonreciprocal devices, especially for integrated on-chip applications. Other recently proposed designs include hybrid schemes that use switching networks in conjunction with SAW delay lines [9] or a parity-time symmetric nonlinear system [6].

Solid phononic crystals (PnCs), as the elastic counterparts of photonic crystals, are a periodic arrangement of elastic scatterers in a host matrix and have been applied in different fields, such as filters [22], demultiplexers [18,23],

*s.darbari@modares.ac.ir

sensors [24], heat transfer [25], energy harvesting [26,27], and resonators [28]. PnCs, consisting of periodic pillars on the substrate, can lead to local-surface-resonance (LSR) band gaps for elastic surface-coupled modes, compared with hole-based PnCs in which only Bragg reflections are responsible for emerging band gaps [29]. The central frequency of the Bragg band gaps is inversely proportional to the lattice constant, wherein the reflection and transmission of the PnC are maximized and minimized, respectively. However, LSR modes originate from coupling of the individual resonances of the scatterers with the surface elastic modes, leading to slower surface-coupled modes and probable opening of lower-frequency LSR gaps in comparison with the bare surface modes, because the elastic energy is delayed by local resonances in the periodic scatterers [30].

It is proved in the literature that using different PnC-based configurations [4,31–34] can lead to nonreciprocity for bulk or Lamb acoustic waves. However, most of these designs are based on total band gaps of bulk waves in two-dimensional (2D) PnCs that consist of infinite or very long pillars and holes, and they are not applicable to nonreciprocity in high-frequency SAWs for two reasons. (i) The surface band gaps in SAW PnCs are not total gaps and cannot block the elastic energy transmission completely due to the allowed bulk elastic modes. SAW PnCs mostly consist of 2D periodic surficial pillars and holes with subwavelength heights that can lead to partial band gaps for surface-coupled modes. Therefore, previously reported bulk PnC-based nonreciprocal designs are not applicable to SAW nonreciprocity, resulting in a low transmission contrast between the forward and backward directions. (ii) SAWs are surface elastic waves that are inherently more sensitive to the design parameters than bulk waves. This property can deteriorate surface elastic coupling between two PnC halves, leading to low SAW transmission levels, compared with bulk acoustic waves. Thus, just applying the operation principles of previously reported PnC-based bulk acoustic nonreciprocal designs does not work for SAW nonreciprocity with an acceptable rectified transmission signal. This is why there are no reports on successful PnC-based SAW nonreciprocity in the literature.

Here, a monolithic Si-based nonreciprocal SAW device is designed and simulated, which benefits from two different PnCs with an inclined heterojunction in the delay line. Taking advantage of resonating pillars in the PnC and LSR band gaps, we present a miniature device with SAW nonreciprocity in the GHz frequency range. The proposed high SAW nonreciprocity factor is mostly based on the imposed elastic mode conversion in the trapezoidal PnCs with a 45°-inclined cut line, as the dominant physical operation principle. The present report on a PnC-based SAW rectifier proposes a simple, CMOS-compatible, magnetic free, and efficient candidate for on-chip GHz processing, benefiting from very promising output characteristics compared with material-based reports [5,20,21] and structural-based designs [4,31,32,34].

II. THEORY AND IMPLEMENTATION OF SIMULATION

The proposed nonreciprocal SAW structure is composed of two phononic crystals with a heterojunction, each of which is made of Si pillars on Si substrate. The achieved optimized nonreciprocal behavior is designed initially based on the band structure. Therefore, we present the band structures of the PnCs, especially the surface-coupled bands and related elastic modes. For this purpose, we consider a unit cell of the PnC with periodic boundary conditions (PBCs) on all four sidewalls, according to Fig. 1(a). It can be observed that the unit cell consists of the substrate and a cylindrical pillar on top of it. Moreover, to calculate the transmission spectra of the proposed PnCs along the x direction, we consider a supercell with 10 pillars along the wave-propagation direction with PBCs on the lateral sidewalls (along $\pm y$ directions), as shown in Fig. 1(b). Equations (1) and (2) are the coupled equations for solving the propagation of elastic waves [22]:

$$S_{ij} = \frac{1}{2}(\partial_j u_i + \partial_i u_j), \tag{1}$$

$$T_{ij} = C_{ij} S_{ij}, \tag{2}$$

wherein S_{ij}, T_{ij}, $u_{i,j}$, and C_{ij} are the strains, mechanical stresses, atomic displacements, and elastic stiffness components along the $i,j = x,y,z$ directions. It should be noted that the PBCs follow the Bloch-Floquet theorem for elastic waves, so that [35]

$$u_i(x + a, y + a) = u_i(x, y) e^{-i(k_x a + k_y a)}, \tag{3}$$

wherein k_x and k_y are the Bloch wave vectors. For boundaries along the $+z$ direction, we assume a free-surface condition, while along the $-z$ direction we assume fixed and

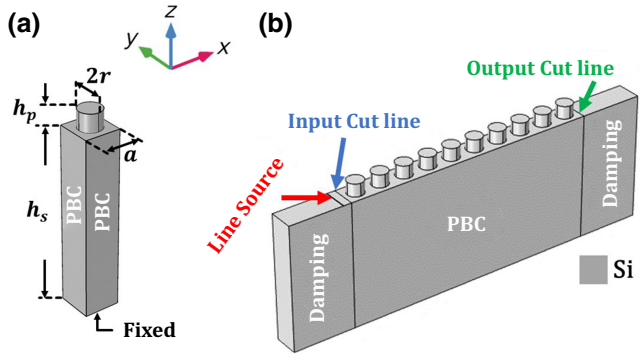

FIG. 1. (a) Unit cell of the PnC used for calculating the related band structure. (b) Supercell of the PnC, with 10 rows of pillars along the wave-propagation direction, used for calculating the transmission spectrum.

low-reflection boundaries in Figs. 1(a) and 1(b), respectively. Moreover, for the front and back sides ($\pm x$ directions) of the supercell in Fig. 1(b), we assume damping layers to minimize wave reflections from these boundaries.

The structural parameters of the investigated PnCs are shown in Fig. 1(a), in which r, h_p, a, and h_s represent the pillar radius, pillar height, lattice constant, and substrate thickness, respectively. It is notable that, to achieve the desired nonreciprocal behavior for SAWs in the GHz frequency range, we use two different lattice constants of $a = 100$ and 200 nm, while assuming fixed $h_p = 100$ nm. Because SAWs are confined to the surface and penetrate to a depth of about one wavelength from the top surface of the substrate [36], we assume a substrate thickness 5 times greater than the larger lattice constant ($h_s = 1$ μm) to decouple the surface waves from Lamb waves [35]. Finally, considering the crystalline symmetry of Si, we have three independent anisotropic elastic constants of $C_{11} = 165.7$ GPa, $C_{12} = 63.9$ GPa, and $C_{44} = 79.9$ and a mass density of $\rho = 2331$ kg/m^3 for the investigated PnCs [35].

As shown in Fig. 1(b), a line source along the y direction is used at the top surface of the supercell to excite the incident SAWs mechanically. Moreover, the input and output cut lines are shown on the surface, along which the integral of the input and output elastic energies are calculated by Eq. (4); the transmission value is achieved from the ratio of the calculated output-to-input elastic energies:

$$T = u_x^2 + u_y^2 + u_z^2. \tag{4}$$

To investigate the transmission behavior of the proposed structure, we should consider two polarizations:

(1) The sagittal-polarized surface source with displacement components of u_x and u_z (in the x-z plane), which leads to excitation of Rayleigh SAWs.

(2) The shear-polarized source in the y direction with a displacement component of u_y (in the y direction), which leads to excitation of shear horizontal SAWs.

Simulations for numerical calculations of the band structures and the transmissions are fulfilled by using the finite-element method.

III. THE BASIC OPERATIONAL BEHAVIOR

Figures 2(a) and 2(b) show the achieved band structures in the first Brillouin zone of PnCs with pillar radii and lattice constants of $r_L = 40$ nm and $a_L = 100$ nm for the left PnC, and $r_R = 85$ nm and $a_R = 200$ nm for the right one. The inset in (b) shows the first Brillouin zone for the square lattice of both PnCs. The dark-blue regions in the band structures cover the bulk modes, while the lower-frequency colored bands on the white background show the surface bands. The interface between the dark-blue and white regions is the sonic cone, which is the boundary between the bulk and surface bands. In other words, the sonic cone represents the bulk modes with minimum group velocities, and thus, separates the bulk modes from the surface modes with lower velocities. Moreover, we present the sagittal-to-shear polarization ratio of the surface modes at each wave vector by the band color. This ratio is calculated by dividing the maximum sagittal-displacement component to that of shear displacement [$\max(u_z,u_x)/\max(u_y)$] for each point in the band structure. Furthermore, the surface bands of the bare substrate are calculated and superimposed in both band structures of Figs. 2(a) and 2(b), which are shown by dashed colored bands. To calculate the surface bands of the bare substrate, we remove the pillars from the unit cell in Fig. 1(a) and calculated the band structure. It is observable in these figures that the first substrate's surface band is sagittal polarized in the Γ-X direction. Moreover, it can be observed that the surface-coupled bands in these PnCs have a lower slope than those of the surface modes for the bare substrate, which means that the surface elastic waves are slowed down in the presence of pillars, as local resonators. This observation is attributed to the creation of surface-coupled modes or LSR modes for these PnCs, in which the resonating pillars are coupled to the substrate surface. Partial local resonance of the surface wave in the pillars is the main reason for the observed reduced wave velocity for the PnCs. Figure 2(c) displays the displacement profile at some selected modes (points A to E) in Fig. 2(b). In this figure, points A and D are related to the first and third surface-coupled modes at X and M points with frequencies of 6 and 10.5 GHz, respectively. Point B (C) is related to the second (first) surface band of the PnC (bare substrate) at a frequency of 6.8 GHz, while point E demonstrates the bulk mode at 16 GHz to elaborate the difference between the displacements of surface and bulk modes. The total displacements (u) related to these points are shown in Fig. 2(c), wherein the surface-coupled elastic modes of the PnC at A, B, and D are mostly confined to the pillars and show very shallow penetration into the substrate. However, for the bulk mode at E, the elastic mode is delocalized, and the displacement profile is distributed throughout both the pillars and whole-substrate thickness of the unit cell. On the other hand, for the pillarless substrate at point C, the surface mode is confined to about the top 200 nm of the substrate, but the penetration depth of the surface mode is absolutely larger than that of the surface-coupled modes (A, B, D). This figure manifests the difference between the surface-coupled modes in the presence of local resonators (pillars) and the pure surface modes when the top pillars are absent. Moreover, the displacement components for points B and C are shown along the x (u_x), y (u_y), and z (u_z) directions in Figs. 2(d) and 2(e), respectively (at 6.8 GHz). As shown in Fig. 2(d), for the second surface-coupled band at B, u_y and u_z are dominant components, and this mode is considered to be a shear-polarized mode, a fact that we

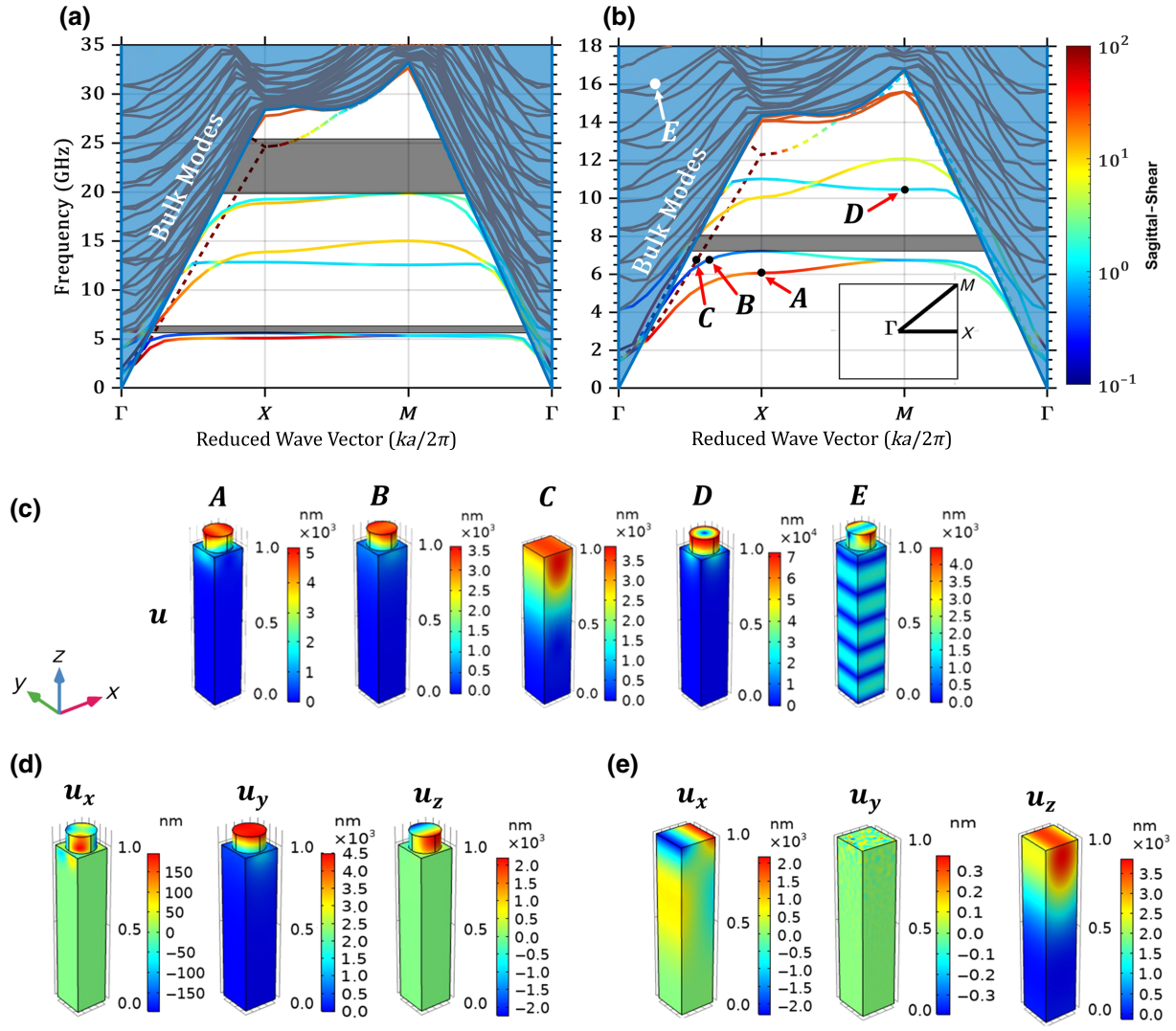

FIG. 2. Calculated band structure for the unit cell with (a) $r_L = 40$ nm and $a_L = 100$ nm and (b) $r_R = 85$ nm and $a_R = 200$ nm. Inset in (b) shows the first irreducible Brillouin zone of the square lattice. Dashed bands in both band structures show surface bands of the bare substrate. (c) Profiles of total displacements (u) for points A, B, C, and D in (b). Displacement components along x (u_x), y (u_y), and z (u_z) directions for (d) point B and (e) point C.

represent by the blue color of the band at this point, according to the color bar. Figure 2(e) illustrates the displacement components of the first surface band of the substrate at C, revealing that sagittal components (u_x and u_z) are dominant compared with the y component of displacement, which is represented by the red color of the dashed band at point C. To elaborate the polarization behavior of the surface-coupled modes in PnCs, for instance, at mode B in Fig. 2(b), we can determine a sagittal-to-shear ratio of 0.48 from the color bar, which is in agreement with the presented max(u_z):max(u_y) ratio in Fig. 2(d) and means that shear polarization is dominant at this point. As shown in Figs. 2(a) and 2(b), the first and second surface-coupled bands in the Γ-X direction of the PnC are overall sagittal and shear bands, respectively. Moreover, it can be observed that, as the slope of the band increases (decreases), the mode polarization is converted into sagittal (shear). The other noteworthy observation is that, when two surface bands approach each other, similar to the third and fourth bands along the Γ-X direction in Fig. 2(a) and along the X-M direction in Fig. 2(b), polarization exchange occurs between the bands.

Considering the presented band structures in Figs. 2(a) and 2(b), we expect different transmission spectra for the PnCs investigated at different directions. Therefore, nonreciprocal transmission behavior can be achieved by engineering the PnC structures and related band structures. For example, in Fig. 2(a), there are surface-coupled bands in both the Γ-X and Γ-M directions at a frequency of 12 GHz, while in Fig. 2(b) transmission is forbidden at

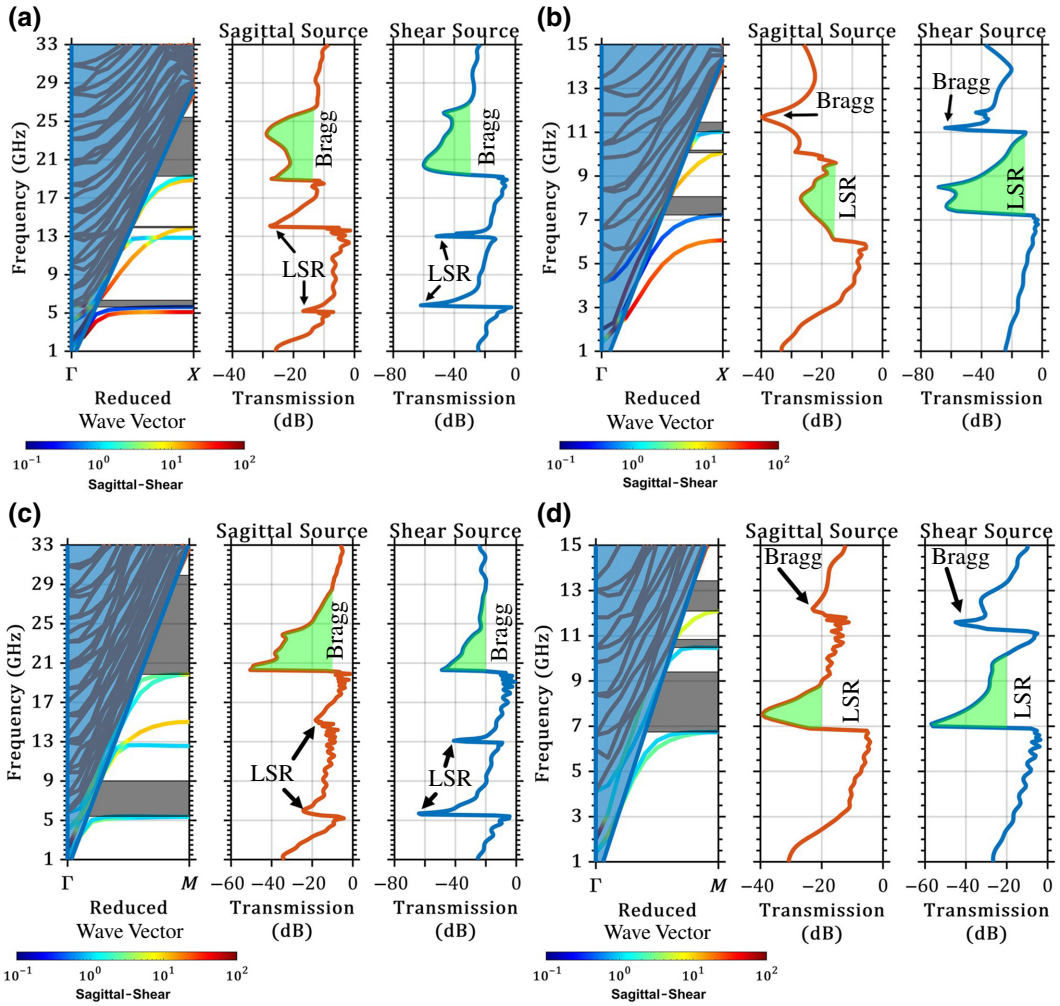

FIG. 3. Calculated reduced band structures along Γ-X and Γ-M directions, in addition to sagittal and shear transmission spectra for perfect PnCs with (a),(c) $r_L = 40$ nm and $a_L = 100$ nm, and (b),(d) $r_R = 85$ nm and $a_R = 200$ nm.

this frequency because surface bands are absent in the Γ-X direction. Moreover, two surface band gaps are observed in Fig. 2(a) with gap-center frequencies of 6 and 22.5 GHz, which are shown by gray bars. The lower-frequency gap is a LSR band gap between the surface-coupled bands, which, in turn, originate from the elastic coupling between discrete resonances of pillars and the surface modes of the substrate. LSR band gaps are strongly dependent on the structural properties of pillars, such as height and radius, but do not change significantly upon changing the lattice constant. The upper gray band gap in Fig. 2(a) is dominantly a Bragg gap with a central gap frequency (f_c) that is determined by the SAW velocity (v) and lattice constant (a) of the PnC through the relationship $f_c v/2a$. Similarly, we investigate the band structure in Fig. 2(b), in which one LSR band gap is observed at 7.5 GHz (shown by a gray bar). Then, we investigate the transmission spectra for the sagittal- and shear-polarized sources, using the supercell illustrated in Fig. 1(b). Figure 3 shows the reduced band structures in the Γ-X direction in addition to the calculated transmissions for PnCs with $r_L = 40$ nm and $a_L = 100$ nm in (a) and $r_R = 85$ nm and $a_R = 200$ nm in (b). We illustrate the partial band gaps in the presented reduced band structures as gray bars. It is observable that the achieved transmissions are in agreement with the previously discussed band structures and displacement polarizations in Figs. 2(a) and 2(b). Moreover, it can be observed in Fig. 3 that Bragg band gaps in (a) are broader than those of (b), while the opposite behavior is observed for LSR band gaps in these two parts of the figure. This observation is in accordance with the Bragg and LSR gaps in the band structures of Figs. 3(a) and 3(b). The other noteworthy observation is that the shear transmissions show deeper LSR band gaps with lower transmission values, compared with the sagittal transmissions. We believe that the negligible x component of the shear modes along the wave-propagation direction (x-direction) leads to a weaker elastic coupling between pillars, making the shear-wave

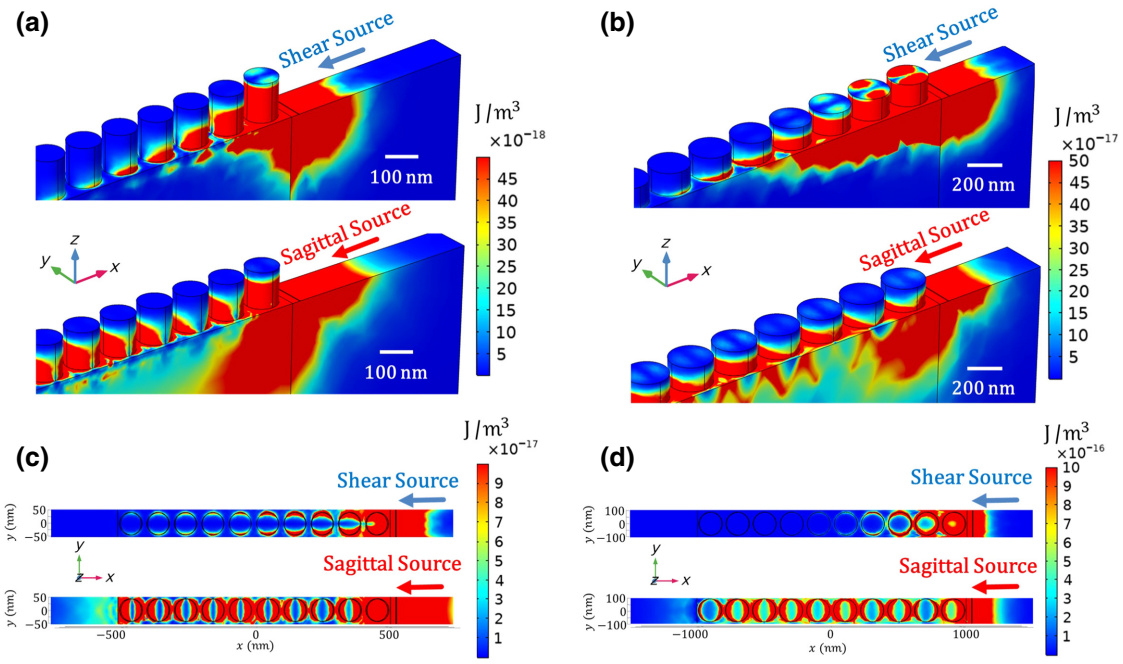

FIG. 4. Profile of stored elastic energy in supercells with (a),(c) $r_L/a_L = 40/100$ (nm/nm) at 6 GHz and (b),(d) $r_R/a_R = 85/200$ (nm/nm) at 7.5 GHz. (a),(b) 3D views; (c),(d) top views of the elastic energy distribution for shear and sagittal sources, respectively.

propagation slower and the shear bands flatter (less dispersive) in comparison with the sagittal bands. The flatter shear bands, as the upper and lower extremes of the LSR band gap in shear transmissions, are the main reason for achieving deeper shear gaps with lower transmission values. These deep LSR gaps in shear transmissions are beneficial for achieving greater nonreciprocal transmission behavior in our designed PnC structure. Therefore, we focus on shear waves in the rest of simulation results in this paper. Moreover, Figs. 3(c) and 3(d) display the reduced band structures in the Γ-M direction for the same PnCs as those in Figs. 3(a) and 3(b), respectively. Moreover, the calculated sagittal and shear transmissions for the PnCs are presented beside the corresponding band structures.

To validate our discussion of elastic coupling between the pillars of the PnCs in shear and sagittal modes, we present the elastic energy distribution for the shear- and sagittal-wave propagations at the central frequency of their related LSR gaps. Figure 4(a) shows the three-dimensional (3D) profile of elastic energy for shear and sagittal excitations, within a supercell of $r_L/a_L = 40/100$ (nm/nm) at 6 GHz, while Fig. 4(b) displays the elastic energy profile for $r_R/a_R = 85/200$ (nm/nm) at $f = 7.5$ GHz. For more clarify, in Figs. 4(c) and 4(d) we present the 2D top views of the energy distribution for shear and sagittal modes of the investigated PnCs at the substrate's surface, corresponding to Figs. 4(a) and 4(b). It is known that the resonating pillars in the PnC are elastically coupled to each other through the top surface of the substrate. Thus, higher elastic energy at the substrate surface between neighboring pillars reveals higher elastic coupling between the pillars, which leads to more-disperse surface-coupled bands and a higher wave velocity. As can be observed in Figs. 4(c) and 4(d), for shear excitation, energy coupling between the pillars in the x direction is weaker than the sagittal one. Moreover, the energy is mostly confined to the pillars, compared with the substrate surface in shear mode; however, both pillars and

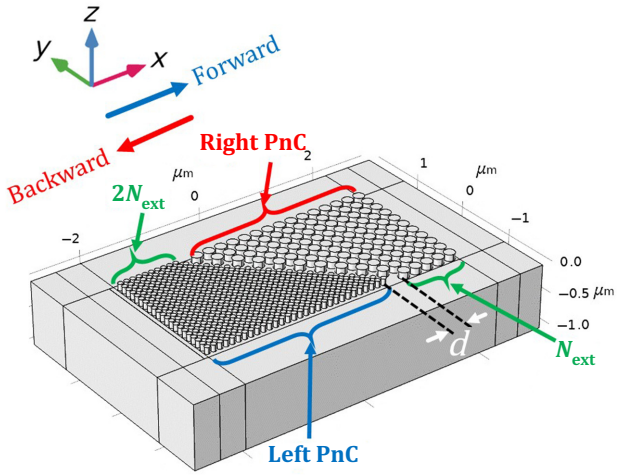

FIG. 5. Proposed nonreciprocal device consists of two PnCs: right PnC with $r_R = 85$ nm and $a_R = 200$ nm and left PnC with $r_L = 40$ nm and $a_L = 100$ nm. Two PnCs are cut at 45° and joined with an interspacing gap of d. Forward excitation is along $+x$ and the backward one is along the $-x$ direction.

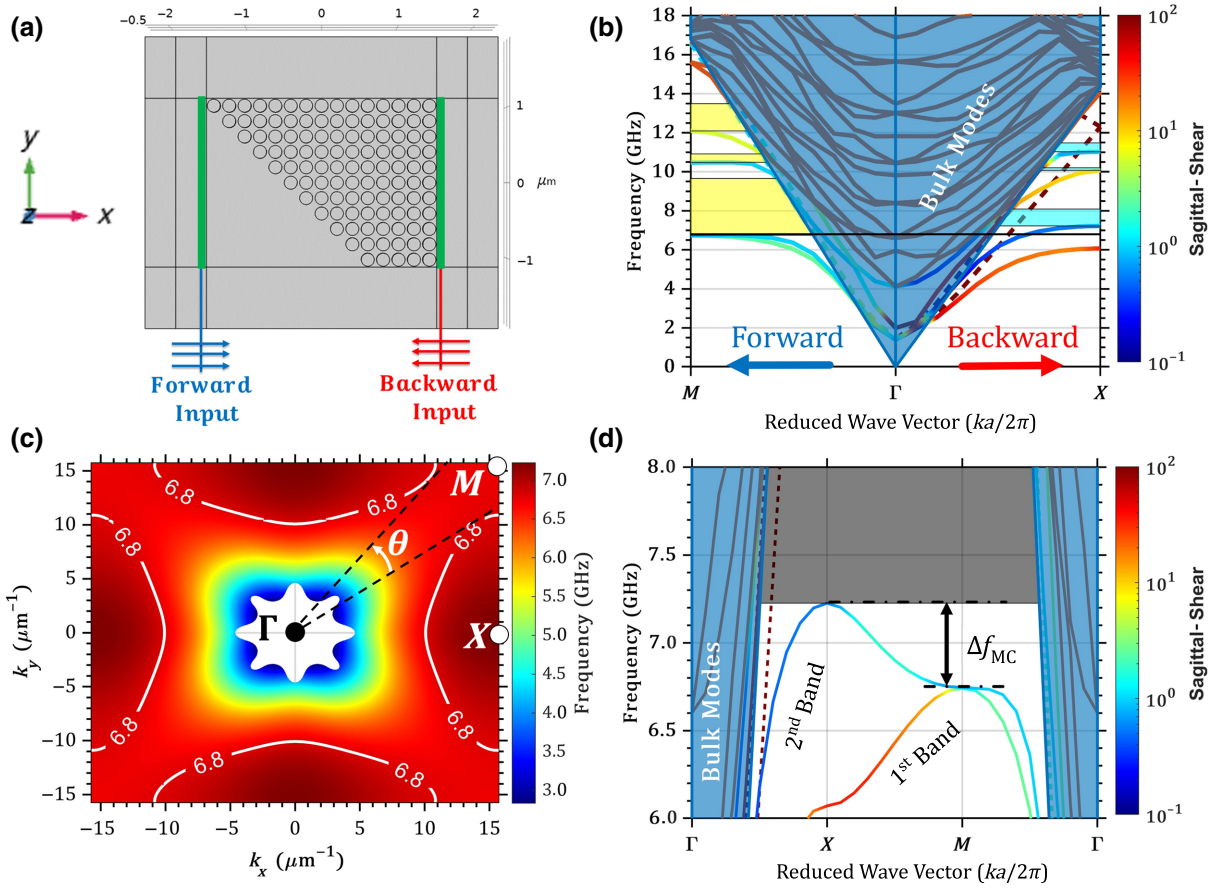

FIG. 6. (a) Scheme of the individual right PnC. (b) Calculated band structure for the right PnC. (c) Isofrequency plot around the second surface-coupled band; (d) magnified band structure around the second surface-coupled band of the PnC.

the substrate surface are involved in the energy distribution of sagittal modes. Hence, we can definitely attribute the observed deeper LSR gaps in shear mode to the proven weaker elastic coupling between resonating pillars. In contrast, as the elastic coupling between neighboring pillars in the PnC increases in sagittal excitation, the sagittal LSR band-gap transmission value increases consequently.

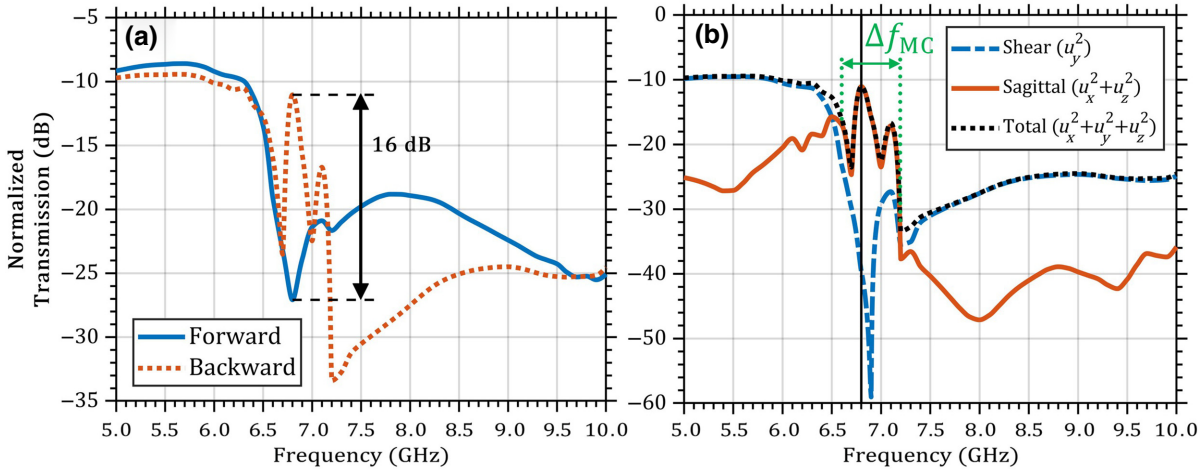

FIG. 7. (a) Normalized transmission spectra for forward ($+x$) and backward ($-x$) shear inputs. (b) Components of the backward transmission in (a) separated into shear ($u_y{}^2$) and sagittal ($u_x{}^2 + u_z{}^2$) components.

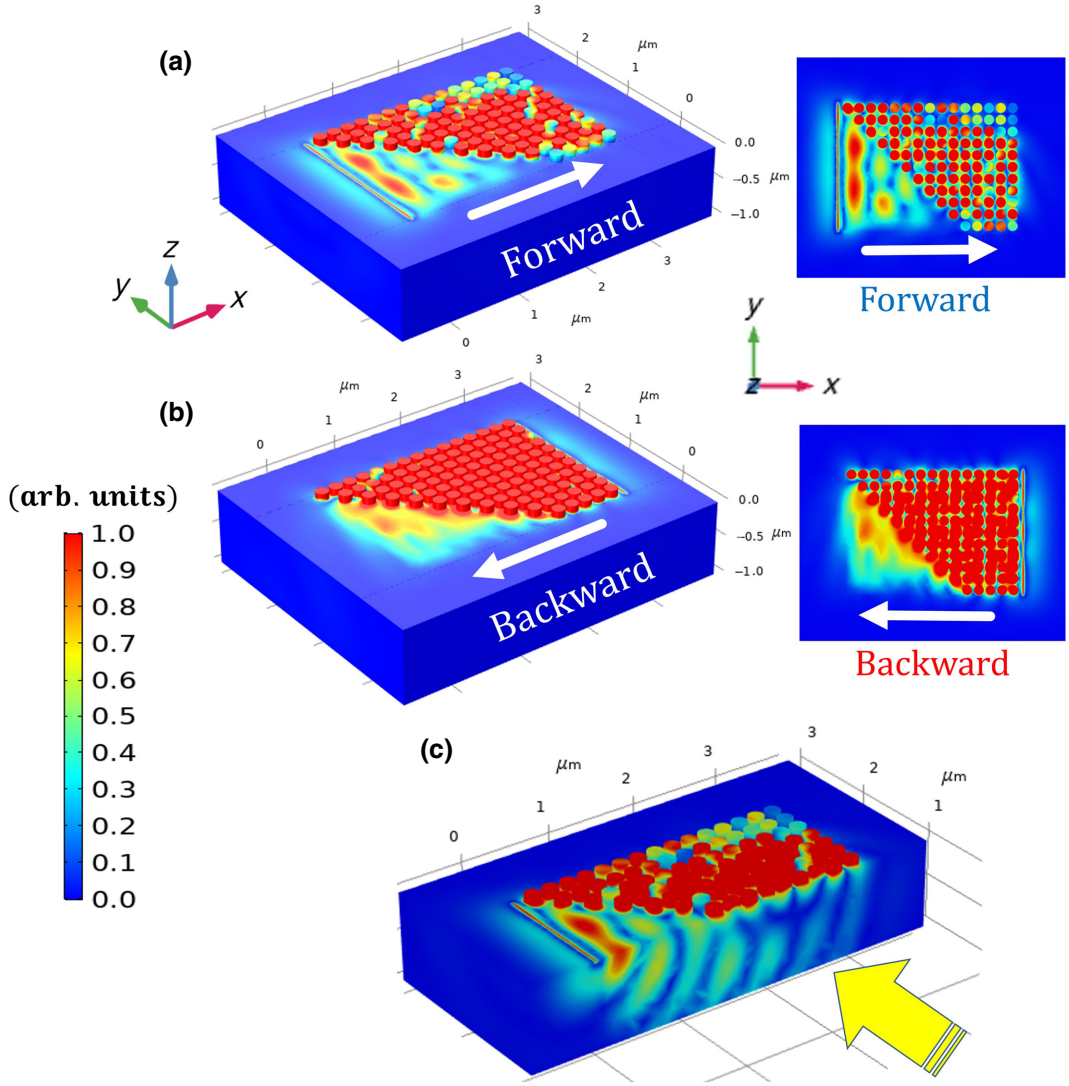

FIG. 8. Total displacement distribution at 6.8 GHz for the right PnC for (a) forward (left, 3D; right, top view) and (b) backward (left, 3D; right, top view) transmissions. (c) Profile of total displacement in the x-z cross section.

IV. THE PROPOSED DEVICE STRUCTURE, NUMERICAL RESULTS, AND DISCUSSION

Figure 5 shows the proposed structure with nonreciprocal SAW behavior, which consists of an inclined heterojunction between two PnCs. The structural parameters of the right PnC, namely, the pillar radius and the lattice constant are $r_R = 85$ nm and $a_R = 200$ nm, respectively, while those for the left PnC are $r_L = 40$ nm and $a_L = 100$ nm, respectively. Both left and right PnCs have square lattices with a Γ-M heterojunction between them. Moreover, we assume an interspacing gap of d along the x direction between two adjacent unit cells of neighboring PnCs at the heterojunction. Damping conditions are considered for all boundary layers along the x and y directions to avoid reflections, and free-surface and low-reflection boundary conditions are assumed for the top $(+z)$ and bottom $(-z)$ surfaces of the device, respectively. N_{ext} is the number of pillars of the right PnC edge, extending away from the interface. Considering $a_R = 2a_L$ in the proposed structure, we assume the number of extended pillars in the left PnC edge to equal $2N_{\text{ext}}$, to achieve a symmetric structure.

To study the transmission behavior of the proposed nonreciprocal structure, first we investigate the right and left trapezoidal PnCs separately. In this regard, Fig. 6(a) shows the individual right trapezoidal PnC schematially, wherein green lines demonstrate the forward and backward input cut lines along $+x$ and $-x$ directions, respectively. To evaluate the forward and backward transmission spectra, we calculate the transmitted elastic energies through Eq. (4). Our simulation results show that, for pillar numbers larger than 11 along the y direction, reflections from the upper and lower boundary edges of the PnC along the x direction are negligible and do not change significantly upon

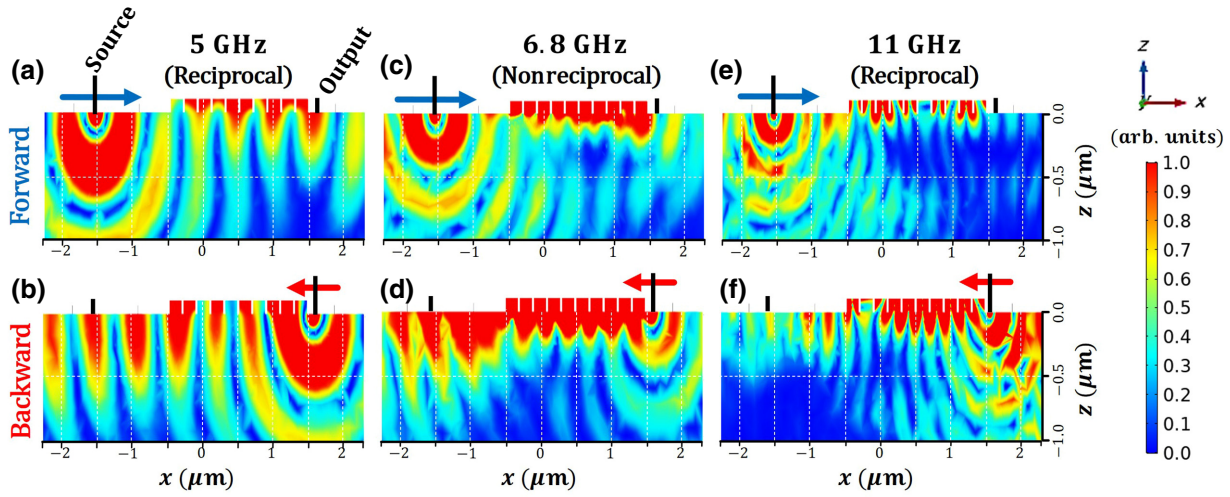

FIG. 9. Total displacement profiles of the right PnC in the x-z plane for forward and backward incident directions at a frequency of (a),(b) 5 GHz, (c),(d) 6.8 GHz, and (e),(f) 11 GHz.

increasing the pillar numbers. Therefore, we assume 11 pillars along the right boundary (along the y direction) of the right PnC to save simulation time. It should be noted that the forward incident surface waves [along the blue arrows in Fig. 6(a)] are coupled to the PnC bands along the Γ-M direction of the dispersion, because of the 45°-inclined left cut line of the right trapezoidal PnC. Therefore, we assume the forward input to be the Γ-M incident direction for the right PnC, equivalently. To validate this assumption numercially, we perform some simulations (not shown here) and find the SAW transmission spectra of a perfect PnC along the Γ-M and Γ-X directions, in accordance with the forward and backward transmission spectra of the right trapezoidal PnC in Fig. 6(a).

The backward incident direction [red arrows in Fig. 6(a)] corresponds to the Γ-X incident direction with respect to the illustrated PnC structure. Figure 6(b) indicates the reduced band structure of the right perfect PnC along the Γ-M and Γ-X directions, wherein the partial band gaps are shown by yellow and cyan bars, respectively. Here, solid colored bands are the surface-coupled bands of the PnC, and the dashed band shows the surface band of the bare substrate. The black horizontal line highlights the specific frequency of 6.8 GHz in the band structures, which corresponds to a surface-coupled shear band in the backward excitation (Γ-X direction). However, in the forward excitation (Γ-M direction), this frequency lies in the low-frequency LSR band gap (bottom yellow gap). Considering this observation in the band structure, we expect nonreciprocal behavior for SAWs at $f = 6.8$ GHz, because wave transmission is forbidden in the forward direction, while it is allowed to propagate through the PnC in the backward direction. Then, to elaborate wave propagation, in Fig. 6(c), we plot the isofrequency plot in a unit cell of this PnC, which is calculated from the intersection of constant-frequency planes with the dispersion surface of a specific mode in the band stucture of Fig. 6(b). It is evidently observable here that isofrequency contours related to $f = 6.8$ GHz show anisotropic behavior with respect to the wave-vector direction, so that they cross with the incident wave vectors of $k_y = 0$, while they do not cross with the incident wave vectors of $k_x = k_y$. This observation reveals the inherent nonreciprocal transmission behavior of the investigated individual right trapezoidal PnC in response to SAWs. As can be seen in the band structure [Fig. 6(b)], frequencies below about 4 GHz lead to bulk modes (dark-blue region) and do not correspond to any allowed surface bands. The white region in the isofrequency plot represents the bulk modes of the PnC related to frequencies below about 4 GHz. Moreover, if we increase the input frequency from 6.8 GHz to about 7.2 GHz, we have allowed bands in the backward direction (in the Γ-X direction); in contrast, we go deeper in the LSR gap of the forward direction (yellow gap in the Γ-M direction). This behavior in the band structure is reflected in Fig. 6(c) by shrinkage of the isofrequency contours towards $k_y = 0$ and pure k_x values, so that incident wave vectors with $k_y \neq 0$ do not cross with those isofrequency contours. In other words, incident wave vectors along the Γ-M direction become completely forbidden. Regarding a similar trend, input frequencies higher than about 7.2 GHz do not correspond to any surface-coupled bands in the band structure of both Γ-M and Γ-X directions [Fig. 6(b)], which corresponds to the disappearence of the allowed isofrequency contours in Fig. 6(c).

As shown in Fig. 6(c), the right trapezoidal PnC shows mode-conversion behavior for cut lines that lie in a radial range of θ around 45° (Γ-M) at $f = 6.8$ GHz, because in this range (shown by dashed black lines) there is no intersection with the related isofrequency countor of the second

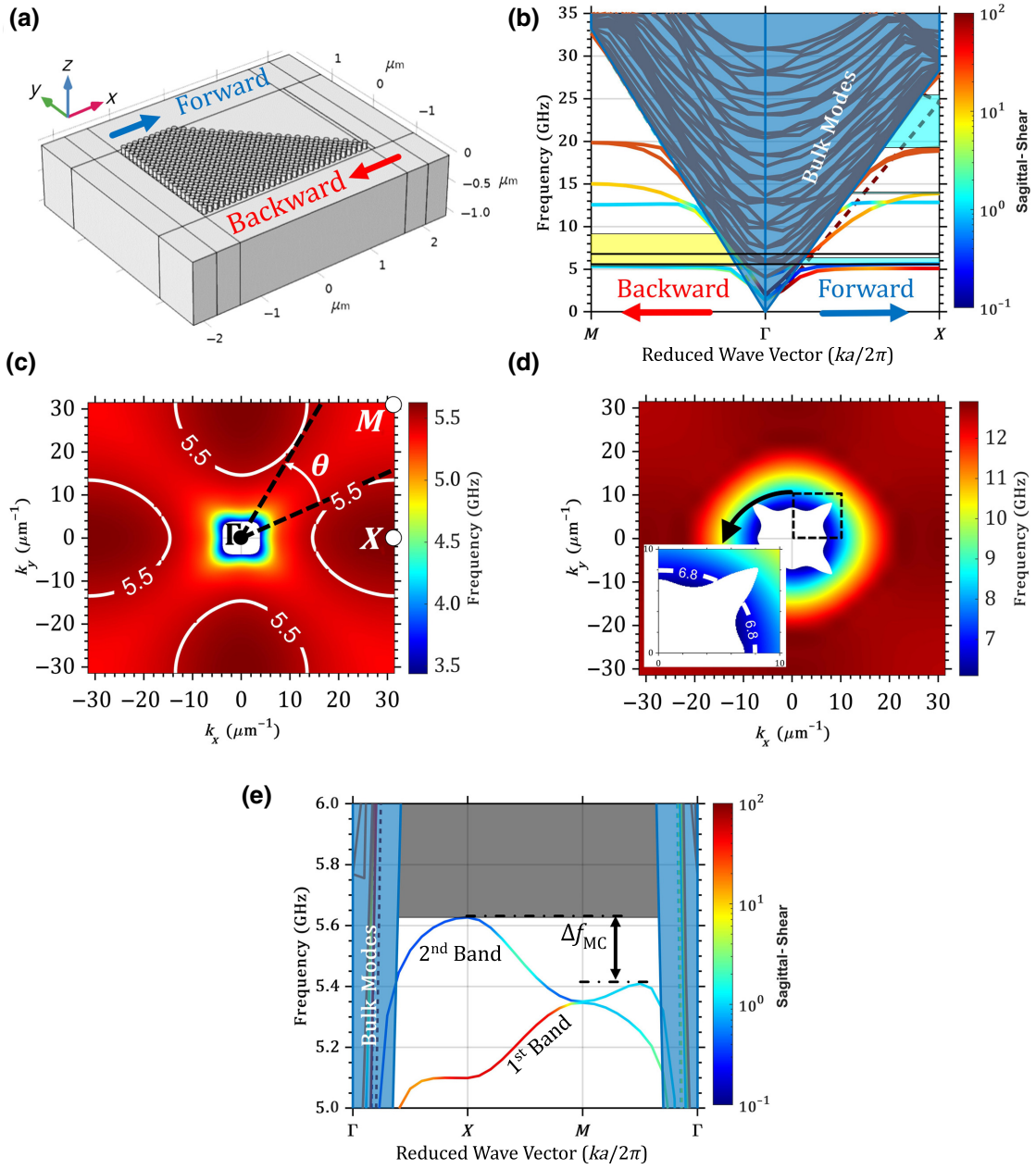

FIG. 10. (a) Individual left PnC and (b) related band structure. (c),(d) Isofrequency plots around the second and third bands of the left PnC, and (e) corresponding magnified band structure.

band. On the other hand, for the fixed cut-line degree of 45° in this PnC, we can expect SAW nonreciprocity in the frequency range from about 6.7 to 7.2 GHz, near to the edge of the upper band gap, wherein the second band shows a relative maximum in the X point, so that no allowed surface-coupled band exists in the Γ-M direction.

Figure 7(a) demonstrates shear forward-backward transmission spectra of the right trapezoidal PnC. Here, the exerted input source is assumed to be shear polarized, while all displacement components at the output are considered for the transmission calculations. In this figure, we observe that the backward transmission value is about 16 dB higher than the forward transmission value at an input frequency of 6.8 GHz, which reveals the maximum nonreciprocal behavior of the right trapezoidal PnC. Moreover, the backward transmission value at this nonreciprocal frequency is -11 dB, while the forward transmission is approximately forbidden. Then, to elaborate the backward transmission behavior, we demonstrate the decoupled sagittal $(u_x{}^2 + u_z{}^2)$ and shear $(u_y{}^2)$ components of the backward transmission, in addition to the total backward transmission of the right trapezoidal PnC in Fig. 7(b),

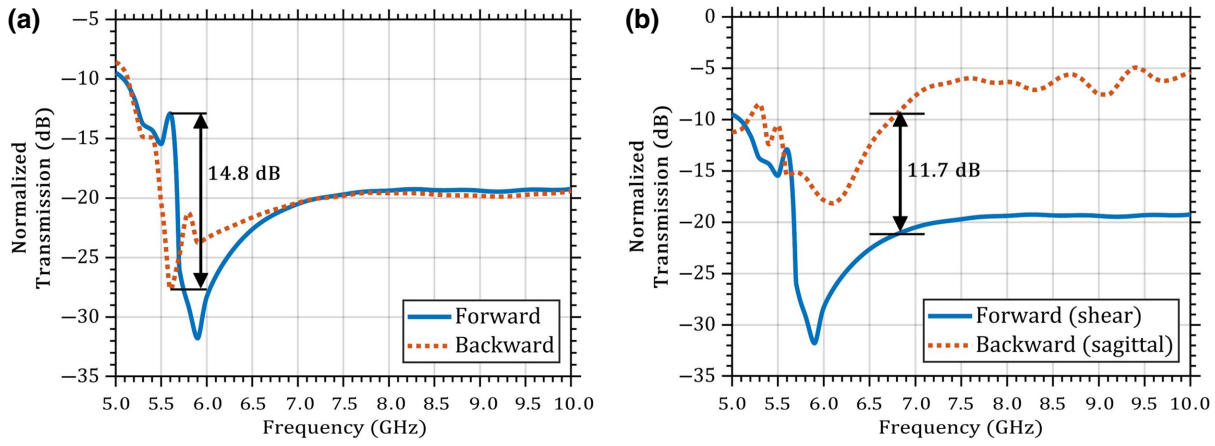

FIG. 11. Normalized transmissions in the left PnC for (a) forward and backward shear-polarized input and (b) forward (backward) shear- (sagittal-) polarized input.

wherein the proposed nonreciprocal frequency is highlighted by a vertical black line. It can be observed that a polarization-conversion phenomenon occurs at the nonreciprocal frequency. In other words, the incident backward shear-polarized excitation is converted into a pure sagittal-polarized elastic wave, so that the sagittal component is about 30 dB higher than that of the shear component of the backward transmission. This polarization conversion is a key physical origin of the proposed SAW rectifying behavior based on the PnC structure. To better understand this phenomenon, one should consider the backward transmission of the trapezoidal PnC in Fig. 6(a). As discussed in Fig. 6(d), the backward incident wave is coupled to the PnC in the Γ-X direction and exits from the 45° cut line, along the Γ-M direction. However, the PnC does not support any surface-coupled band at this frequency ($f = 6.8$ GHz) and direction. Therefore, the wave is partially diffracted along the 45° cut line. As shown in Figs. 2(d) and 2(e), the right PnC supports a surface-coupled mode with u_y and u_z displacement components, while the bare substrate supports sagittal surface modes with u_x and u_z displacement components at $f = 6.8$ GHz. Therefore, the backward elastic wave in the right trapezoidal PnC is coupled to the surface band of the substrate with dominant displacement of u_z at the output cut line, converting into a sagittal polarization consequnetly. As indicated in Fig. 6(d), this phenomenon occurs for the right trapezoidal PnC with a 45° cut line in a frequency range of $\Delta f_{\mathrm{MC}} = 0.5$ GHz, which is in complete agreement with the mode-conversion frequency range in the calculated transmission spectrum of the right trapezoidal PnC in Fig. 7(b). It should be emphasized that, for a perfect PnC, there is no mode-conversion effect, and this behavior arises from the existence of the designed asymmetric left and right cut lines in the propsed trapezoidal PnC under specific conditions. This phenomenon is the reason that the shear SAW input has led to higher nonreciprocity than the sagittal one in our design, because this mode conversion is only allowed for shear-to-sagittal conversion due to the pure sagittal polarization of the bare surface band at $f = 6.8$ GHz.

Figures 8(a) and 8(b) display the total displacement profiles, when the investigated right trapezoidal PnC is exposed to forward and backward shear sources. It is observed that the forward and backward elastic waves pass through the PnC, mostly along the x direction, while reflections from the $\pm y$ boundaries are negligible. It is observable in Fig. 8(b) that the backward incident of the right trapezoidal PnC tends to diffract along the Γ-M direction, showing a slight in-plane wave-vector rotation, and couples to the sagittal surface mode of the substrate. This observation is attributed to Figs. 6(c) and 6(d), where we show that the backward incident wave excites the allowed surface-coupled mode in the Γ-X direction. However, the backward output does not correspond to any allowed mode in the Γ-M direction and couples to the bare surface bands consequently. For more clarification, we demonstrate the forward-displacement profile in an x-z cut plane at the middle of the PnC structure, as shown in Fig. 8(c). In the presented bulk cross section, we can observe that most of the forward incident wave is coupled to the bulk, and the surface-coupled wave is attenuated significantly, which leads to a very low transmission value at the surface output cut line. To elaborate the transmission behavior of the right trapezoidal PnC, we present the 2D displacement distributions in the x-z plane for the forward and backward shear excitations at excitation frequencies corresponding to reciprical and nonreciprocal frequencies, as shown in Fig. 9. For this purpose, we choose frequencies of 5 GHz (parts a and b), 6.8 GHz (parts c and d), and 11 GHz (parts e and f), in turn, corresponding to reciprocal, nonreciprocal, and reciprocal behavior, according to Fig. 7(a). As indicated in Fig. 9, the forward (upper profiles) and backward displacement distributions (lower profiles) lead

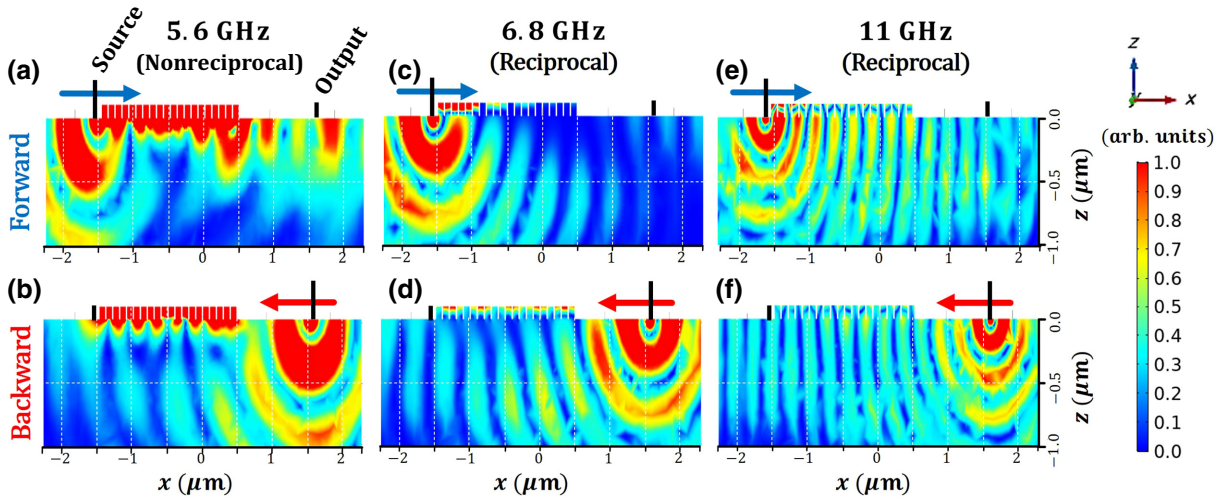

FIG. 12. Total displacement profiles of individual left PnC in the x-z plane for forward and backward incident directions at a frequency of (a),(b) 5.6 GHz, (c),(d) 6.8 GHz, and (e),(f) 11 GHz.

to high surface displacements at the output cut lines for reciprocal frequencies of 5 and 11 GHz. However, for a frequency of 6.8 GHz, the surface output displacement is negligible in forward excitation, as opposed to backward excitation. These strong asymmetric displacement profiles in the forward and backward excitations reveal the nonreciprical behavior of the proposed right trapezoidal PnC for SAWs at $f = 6.8$ GHz. Moreover, the displacement profiles in Fig. 9 clarify the coupling between the pillars and the substrate surface for the allowed transmissions. However, the surface-wave transmission is significantly attenuated, when coupling between the pillars and the surface is weakened, as shown in the forward excitation at $f = 6.8$ GHz. The other noteworthy point is that surface-coupled modes completely emerge in both the forward and backward directions for $f = 5$ GHz, so that both forward and backward transmissions are high. However, for $f = 11$ GHz, surface-coupled waves are disturbed, so that, despite reciprocal transmission, we observe low forward and backward transmissions.

As the next step, we perform a similar study to evaluate the individual behavior of the left trapezoidal PnC in the proposed device structure (Fig. 5). Figures 10(a) and 10(b) show the individual left trapezoida; PnC and the corresponding reduced band structure, respectively.

Here, the forward direction in Fig. 10(a) corresponds to the Γ-X direction, while the backward direction corresponds to the Γ-M direction in the perfect PnC [as shown in the band structure of Fig. 10(b)]. Again, the dashed bands in the band structure of Fig. 10(b) show the first and second surface bands of the bare substrate. Two solid black horizontal lines in Fig. 10(b) represent constant frequencies of 5.6 and 6.8 GHz. It can be observed in Fig. 10(b) that a frequency of 5.6 GHz corresponds to the LSR band gap in the backward direction, while it corresponds to the second surface band of the PnC in the forward direction. Therefore, we expect nonreciprocal behavior for the left trapezoidal PnC at $f = 5.6$ GHz, so that forward transmission is allowed and backward transmission is forbidden. In contrast, a frequency of 6.8 GHz corresponds to the sagittal surface band for the forward direction, while it corresponds to the LSR band gap in the backward direction. Therefore, we expect reciprocal, but highly attenuated, transmission behavior for both the forward and backward excitations, when we apply a shear-polarized source. Figures 10(c) and 10(d) depict the calculated isofrequency plots for the low-frequency surface-coupled bands of the band structure, wherein central white zones represent the bulk modes. Figure 10(c) displays the isofrequency contours for frequencies lower than about 5.63 GHz (second surface band) and confirms the nonreciprocal behavior of the left trapezoidal PnC structure at $f = 5.6$ GHz. It can be observed that the isofrequency contour of $f = 5.6$ GHz indicates completely anisotropic behavior, concerning the allowed forward ($k_y = 0$) and forbidden backward ($k_x = k_y$) transmissions. Figure 10(d) displays the isofrequency contours for frequencies higher than about 6.5 GHz (third surface band), wherein we can observe a sagittal and isotropic contour for $f = 6.8$ GHz, denoting a nearly equal elastic wave velocity in all directions. Moreover, the inset in Fig. 10(d) shows a magnified view of the dashed rectangle zone in this figure, wherein we can observe the allowed forward transmission for surface-coupled modes in the Γ-X direction ($k_y = 0$) at 6.8 GHz. However, the inset clarifies that the backward surface excitation is mainly converted into the bulk mode (enters the white zone) for the Γ-M incident direction ($k_x = k_y$).

According to the magnified band structure in Fig. 10(e), the second surface-coupled band is a shear band along Γ-X with a relative maximum at point X. Similar to Fig. 6(d),

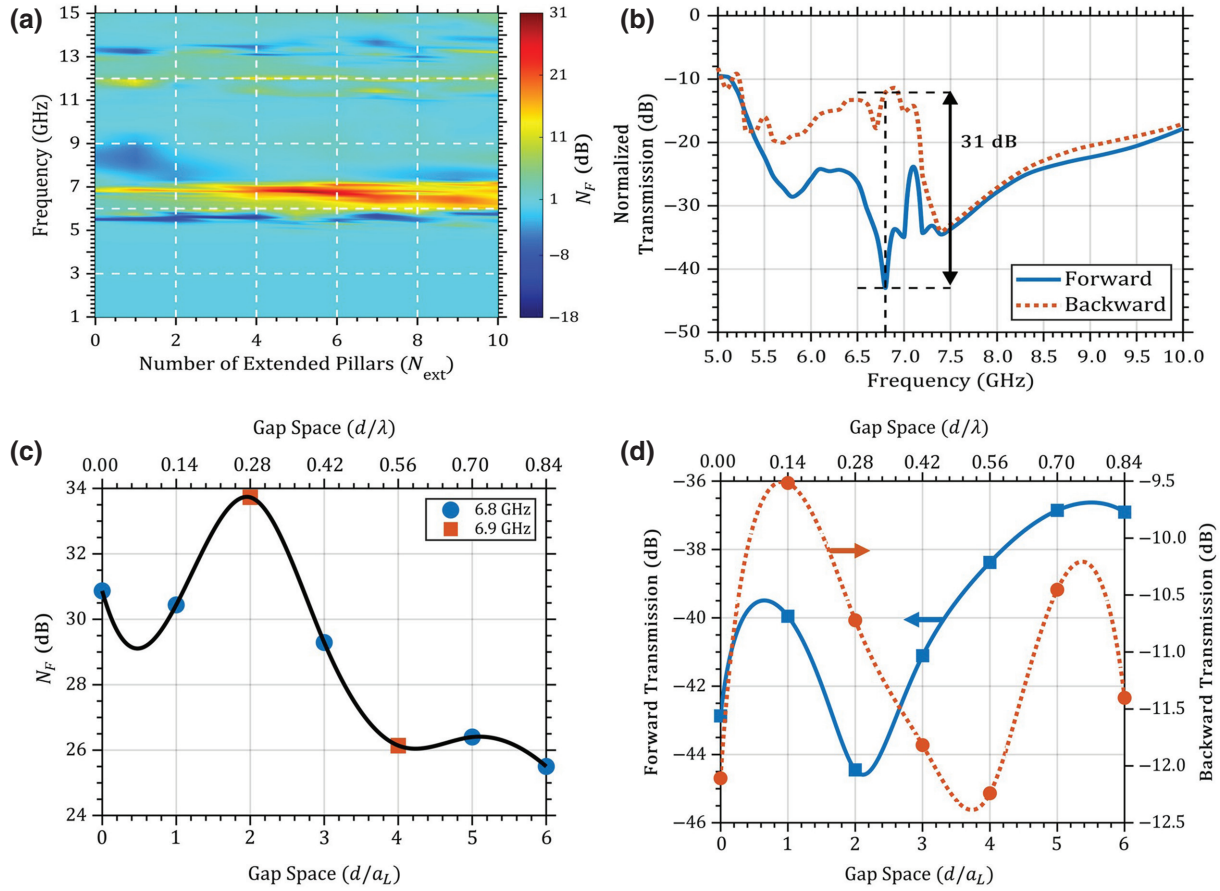

FIG. 13. Simulation results of the proposed device. (a) Spectrum of calculated N_F versus varying N_{ext} for $d = 0$. (b) Forward and backward transmission spectra with $N_{\text{ext}} = 5$ and $d = 0$. (c) Variation of calculated N_F versus d value. (d) Forward and backward transmission values versus d.

this dispersion behavior leads to a mode-conversion frequency range of Δf_{MC}, wherein there is no guided mode in the Γ-M direction. Therefore, the forward incident wave of the left trapezoidal PnC tends to diffract along the Γ-M direction, showing a slight in-plane wave-vector rotation, and couples to the sagittal surface mode of the substrate. Therefore, a mode conversion is expected from a frequency of 5.41 GHz to about 5.63 GHz, corresponding to a mode-conversion frequency range of $\Delta f_{\text{MC}} = 220$ MHz for the left trapezoidal PnC with a 45°-inclined cut line. On the other hand, the left trapezoidal PnC shows mode-conversion behavior for cut lines that lie in a radial range of θ around 45° at $f = 5.6$ GHz, as shown in Fig. 10(c).

Then, we present the calculated forward and backward transmissions of the left PnC for the shear-polarized excitation in Fig. 11(a), which confirms the previous discussions based on the related band structure and isofrequency plots [Figs. 10(b)–10(e)]. As shown in Fig. 11(a), we achieve a maximum nonreciprocity of +14.8 dB at $f = 5.6$ GHz, with a maximum forward transmission of −12.89 dB. The other noteworthy point is that the backward incident wave first enters the right trapezoidal PnC in the proposed complete device structure (Fig. 5), and then enters the left trapezoidal PnC. On the other hand, we discussed for Fig. 7 that the backward shear-polarized incident wave is converted into a sagittal wave at $f = 6.8$ GHz, while passing through the right PnC. Thus, we should consider the sagittal-polarized excitation source for the left PnC, to elaborate the backward shear transmission behavior of the total structure with the 45°-inclined PnC heterojunction at this frequency. Regarding this, in Fig. 11(b), we plot the calcuated shear incident forward transmission, superimposed with the sagittal-polarized backward transmission of the individual left trapezoidal PnC. It can be observed that, for frequencies above 5.6 GHz, the individual left PnC starts the nonreciprocal behavior, so that nonreciprocity approaches 11.7 dB at $f = 6.8$ GHz. Data present in Fig. 11(b) help to better explain the transmission behavior of the total heterojunction PnC structure. Considering numerical investigations of the individual right and left trapezoidal PnCs at $f = 6.8$ GHz (Figs. 6–11), we expect that the shear-polarized forward incident wave to the complete PnC-based heterostructure (Fig. 5) first passes through the left PnC, then couples to the right PnC,

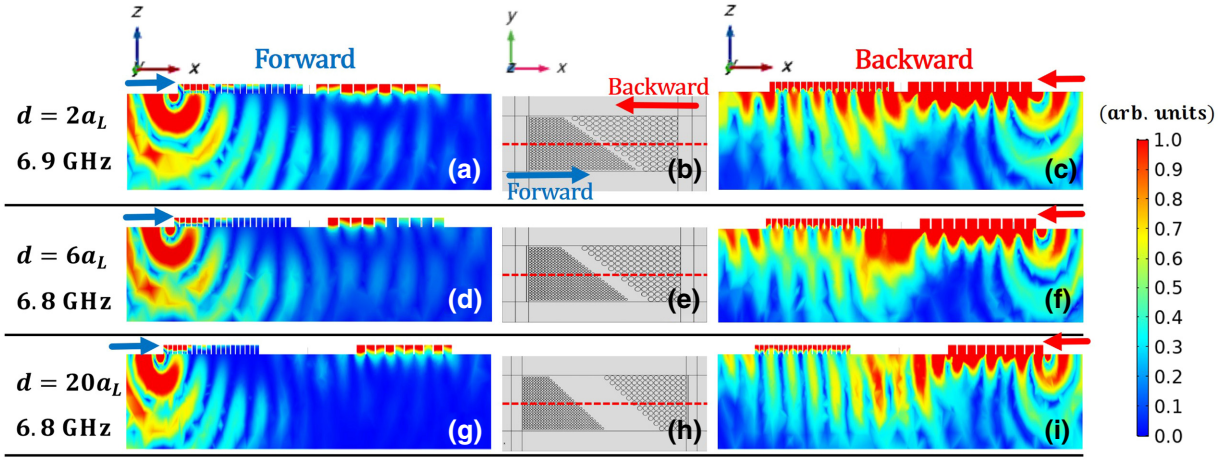

FIG. 14. Forward displacement, top-view scheme, and backward displacement for (a)–(c) $d = 2a_L$ at 6.9 GHz, (d)–(f) $d = 6a_L$ at 6.8 GHz, and (g)–(i) $d = 20a_L$ at 6.8 GHz.

and passes through without significant polarization conversion, but shows considerable attenuation. However, we expect that the shear-polarized backward incident wave to the complete heterostructure first converts into sagittal mode while passing through the right PnC, then successfully passes through the left PnC, and it shows a significant backward transmission. In other words, we expect a high backward transmission compared with the forward transmission at $f = 6.8$ GHz for the proposed PnC-based heterostructure.

To complete studying the behavior of the left trapezoidal PnC, in Fig. 12, we show the total displacement distribution at a nonreciprocal frequency of 5.6 GHz [parts (a) and (b)], in addition to two other reciprocal frequencies of 6.8 and 11 GHz [parts (c)–(f)]. All displacements are demonstrated in the x-z cross section of the left PnC

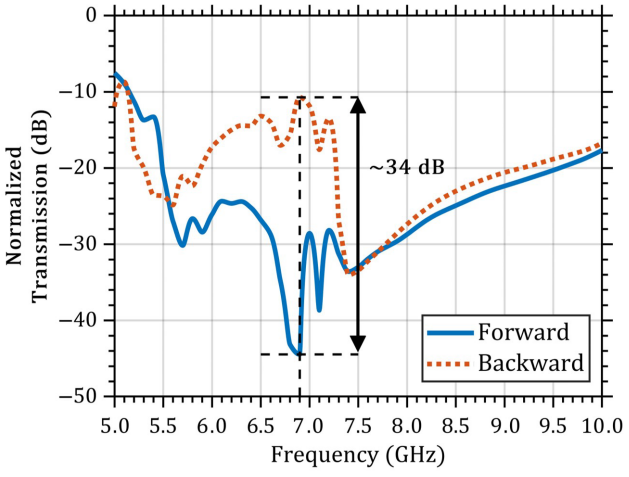

FIG. 15. Forward and backward transmission spectra in the designed nonreciprocal device with structural parameters listed in Table I.

and are related to the shear-mode input. As shown in this figure, the incident elastic wave transmits through the left PnC by surface-coupled resonances with the pillars, which are apparently observable for the forward transmission at $f = 5.6$ GHz. However, the backward incident wave at $f = 5.6$ GHz remains confined to the pillar resonances, so that a small portion of the elastic wave is transmitted to the output cut line, leading to nonreciprocal behavior. At $f = 6.8$ GHz, it can be seen in Fig. 12(b) that the forward incident wave leads to resonances in pillars and decays along the x direction, becoming decoupled from the surface elastic modes. However, for the backward incident wave, despite the resonances in the pillars, the elastic wave is mostly coupled to the bulk, as observed in Fig. 12(d), so that no significant nonreciprocity is achieved here. For higher frequencies, such as 11 GHz, no elastic localization is observed in the pillars, and the energy is transmitted through out the whole cross section with reciprocal behavior.

Considering the aforementioned results regarding the transmission behavior of individual right and left trapezoidal PnCs, significant nonreciprocal behavior is expectable for the complete PnC-based proposed heterostructure device at $f = 6.8$ GHz. Figure 13(a) shows the calculated spectrum of the nonreciprocity factor [N_F (dB) $= 10 \log_{10}$(backward transmission/forward transmission)] versus the number of extended pillars (N_{ext}) in the proposed heterostructure device, when the interspacing gap (Fig. 5) is $d = 0$. As it is shown, a significant N_F is achieved at $f = 6.8$ GHz, and it is enhanced for $N_{\text{ext}} > 3$, due to the hindered direct coupling between incident excitation and the output port. The N_F is maximized for $N_{\text{ext}} = 5$, meaning that five extended pillars are adequate for blocking direct elastic coupling between the input incident wave and output cut line. Hence, we assume $N_{\text{ext}} = 5$ for the rest of our simulations. Figure 13(b) shows

the forward and backward transmissions of the proposed heterostructure with $N_{ext} = 5$ and $d = 0$, confirming a significant value of $N_F = 31$ dB, with an acceptable backward insertion loss of about 12 dB, at $f = 6.8$ GHz. This significant SAW nonreciprocity at $f = 6.8$ GHz is mainly achieved due to three factors in the presented PnC heterostructure: (i) the difference between the surface-coupled bands of the two PnCs, originating from different pillar radii and lattice constants, and the heterojunction interface that leads to different elastic coupling strength in the forward-backward directions; (ii) the allowed coupling between the surface-coupled modes of the PnC and the surface modes of the bare substrate; and (iii) the allowed polarization conversion in the right PnC from shear to sagittal polarization for the backward incident wave.

After the discussed band-structure engineering, we investigate the effect of the gap space between the left and right PnCs at the heterojunction on the nonreciprocal behavior of the structure. By inserting a gap space (d), as shown in Fig. 5, SAW coupling between two PnCs and the achieved N_F can be changed, consequently. The gap space (d) is defined as the distance between two adjacent unit cells along the x direction and is varied from a_L to $6a_L$. Figure 13(c) shows the calculated maximum N_F value versus the normalized gap space (d/a_L), wherein a maximum nonreciprocity of about 34 dB is achieved for $d = 2a_L$. It is notable that the N_F peak frequency is slightly shifted from 6.8 GHz (for $d = 0$) to 6.9 GHz (for $d = 2a_L$) in the complete heterostructure; this is attributed to modified elastic coupling and acoustic impedances related to the PnCs. In Fig. 13(c), we also display the gap-space values normalized to the elastic wavelength (λ) at the top secondary x axis. The forward and backward transmission values at the maximum N_F value are depicted in Fig. 13(d) versus varying d. As it is shown, the gap-space value shows sinusoidallike effects on the forward and backward transmission values. Figure 13(d) shows that increasing d from zero to a_L or $2a_L$ even leads to increasing the backward transmission value from -12 dB to -9 or -10.68 dB, respectively. Therefore, it is observable that acoustic impedance modulation by varying the gap space in the lattice-constant range can also lead to a decreased insertion loss.

The gap-space effect can be further investigated by the elastic wave distriburion, as shown in Fig. 14. Figures 14(a)–14(c), 14(d)–14(f) and 14(g)–14(i) are related to the proposed heterostructure with different gap spaces equal to $2a_L$, $6a_L$, and $20a_L$, at the excitation frequency of maximum N_F. Figures 14(b), 14(e), and 14(h) indicate the top-view schemes (x-y plane), while the presented elastic wave distributions are related to the forward (left parts) and backward (right parts) excitations in the x-z cross sections along the red dashed lines in the top-view schemes (middle parts). For the forward excitations in Fig. 14, it is shown that the elastic wave decouples from the surface after propagating through the left PnC. However, higher d values can lead to slightly enhanced surface coupling of the forward elastic wave. For backward excitations, the elastic energy is localized inside the gap space between two PnCs for smaller d values. However, this confinement is decreased for higher d values, and more elastic energy dissipates in the bulk substrate.

TABLE I. Parameters of the optimized heterostructure design to achieve the highest N_F and transmission values.

Parameter	Symbol	
Pillar radius of left PnC	r_L	40 nm
Pillar radius of right PnC	r_R	85 nm
Lattice constant of left PnC	a_L	100 nm
Lattice constant of right PnC	a_R	200 nm
Pillar height	h_p	100 nm
Number of extended pillars	N_{ext}	5
Gap space	d	$2a_L = 200$ nm
Substrate thickness	h_s	1 μm

Hence, after optimizing the gap-space value to achieve the maximum N_F value, in addition to the maximum backward transmission value, we assume $d = 2a_L$. Table I presents the final structural parameters of the optimized heterostructure device. As stated before, we assume the same pillar heights in the left and right PnCs throughout the simulations, so that the proposed heterostructure device can be fabricated without involving fabrication complexities or extra costs. Figure 15 indicates the calculated final forward-backward SAW shear transmission spectra for the proposed optimized heterostructure at $f = 6.9$ GHz, wherein $N_F = 34$ dB, and the backward transmission value equals -10.68 dB. Table II summarizes the output results of the proposed optimized nonreciprocal SAW device, compared with other recently reported nonreciprocal SAW devices. According to Table II, our proposed device is a promising candidate as a SAW on-chip rectifier, because of both a high nonreciprocity factor and a low insertion loss. Our device benefits from a simple fabrication process and does not need any external excitation for the achieved desired operation.

TABLE II. Output parameters of the optimized heterostructure device, compared with prevoius reports on nonreciprocal SAWs.

Ref.	Frequency	External excitation	N_F	Insersion loss (dB)
[5]	GHz	Magnetic	20%	...
[20]	GHz	Magnetic	45 dB	20
[21]	MHz	Electrical	2.5 dB	40
Our work	GHz	None	34 dB	10.68

V. CONCLUSION

We propose a GHz nonreciprocal SAW device based on a 45°-inclined heterojunction in PnCs. In this structure, two PnCs with different pillar radii and lattice constants are coupled at a heterojunction interface. The proposed SAW nonreciprocal behavior is based on engineered band structures of the neighboring PnCs, in addition to the induced SAW shear-to-sagittal mode conversion in the right trapezoidal PnC. This mode-conversion phenomenon is the dominant physical behavior that affects and enhances the nonreciprocity, which occurs over a limited frequency range and depends on the incident direction with respect to the inclined cut line of the trapezoidal PnC. Our simulation results show an optimized SAW nonreciprocity as high as 34 dB, along with a transmission value of -10.68 dB at $f = 6.9$ GHz for shear-polarized excitation. This high nonreciprocal behavior is mainly attributed to different responses of the PnCs to different incident directions and the induced polarization conversion that occurs in the trapezoidal PnC with a higher pillar radius. Moreover, by making an interspace gap between the PnCs at the interface, it is shown that the elastic coupling strength between two PnCs is changed, so that both nonreciprocity and transmission values can be enhanced. The proposed nonreciprocal SAW device benefits from a simple fabrication process, without the need for external excitation fields for nonreciprocal behavior, which is suitable for on-chip miniature signal-processing devices in wireless-communication applications.

AKNOWLEDGEMENT

The authors acknowledge financial support from Tarbiat Modares University through Grant No. IG-39703.

[1] C. Caloz, A. Alù, S. Tretyakov, D. Sounas, K. Achouri, and Z.-L. Deck-Léger, Electromagnetic Nonreciprocity, Phys. Rev. Appl. **10**, 047001 (2018).

[2] H. Ren and Y. Xie, Simulations of the multipactor effect in ferrite circulator junction with wedge-shaped cross section geometry, IEEE Trans. Electron Devices **67**, 5144 (2020).

[3] X. Zhou, S. K. Gupta, X. Zhu, G. Su, P. Zhan, Y. Liu, Z. Chen, M. Lu, and Z. Wang, Nonreciprocal Isolation and Wavelength Conversion via a Spatiotemporally Engineered Cascaded Cavity, Phys. Rev. Appl. **13**, 044037 (2020).

[4] A. Cicek, O. Adem Kaya, and B. Ulug, Refraction-type sonic crystal junction diode, Appl. Phys. Lett. **100**, 111905 (2012).

[5] A. Hernández-Mínguez, F. Macià, J. Hernàndez, J. Herfort, and P. Santos, Large Nonreciprocal Propagation of Surface Acoustic Waves in Epitaxial Ferromagnetic/Semiconductor Hybrid Structures, Phys. Rev. Appl. **13**, 044018 (2020).

[6] L. Shao, W. Mao, S. Maity, N. Sinclair, Y. Hu, L. Yang, and M. Lončar, Non-reciprocal transmission of microwave acoustic waves in nonlinear parity–time symmetric resonators, Nat. Electron. **3**, 267 (2020).

[7] M. Xu, K. Yamamoto, J. Puebla, K. Baumgaertl, B. Rana, K. Miura, H. Takahashi, D. Grundler, S. Maekawa, and Y. Otani, Nonreciprocal surface acoustic wave propagation via magneto-rotation coupling, Sci. Adv. **6**, eabb1724 (2020).

[8] B. J. Chapman, E. I. Rosenthal, J. Kerckhoff, B. A. Moores, L. R. Vale, J. A. B. Mates, G. C. Hilton, K. Lalumiere, A. Blais, and K. W. Lehnert, Widely Tunable On-Chip Microwave Circulator for Superconducting Quantum Circuits, Phys. Rev. X **7**, 041043 (2017).

[9] R. Lu, T. Manzaneque, Y. Yang, L. Gao, A. Gao, and S. Gong, A radio frequency nonreciprocal network based on switched acoustic delay lines, IEEE Trans. Microwave Theory Tech. **67**, 1516 (2019).

[10] D. P. Morgan, A history of surface acoustic wave devices, Int. J. High Speed Electron. Syst. **10**, 553 (2000).

[11] P. Delsing, A. N. Cleland, M. J. Schuetz, J. Knorzer, G. Giedke, J. I. Cirac, K. Srinivasan, M. Wu, K. C. Balram, C. Bauerle, and T. Meunier, The 2019 surface acoustic waves roadmap, J. Phys. D: Appl. Phys. **52**, 353001 (2019).

[12] I. Group, IEEE 5G and Beyond Technology Roadmap White Paper (2017).

[13] A. Winkler, R. Brünig, C. Faust, R. Weser, and H. Schmidt, Towards efficient surface acoustic wave (SAW)-based microfluidic actuators, Sens. Actuators, A **247**, 259 (2016).

[14] M. Mahmoud, A. Mahmoud, L. Cai, M. Khan, T. Mukherjee, J. Bain, and G. Piazza, Novel on chip rotation detection based on the acousto-optic effect in surface acoustic wave gyroscopes, Opt. Express **26**, 25060 (2018).

[15] C. Wang, C. Wang, D. Jin, Y. Yu, F. Yang, Y. Zhang, Q. Yao, and G.-J. Zhang, AuNP-amplified surface acoustic wave sensor for the quantification of exosomes, ACS Sens. **5**, 362 (2020).

[16] D. A. Golter, T. Oo, M. Amezcua, K. A. Stewart, and H. Wang, Optomechanical Quantum Control of a Nitrogen-Vacancy Center in Diamond, Phys. Rev. Lett. **116**, 143602 (2016).

[17] M. M. Mehrnegar, S. Darbari, H. Ramezani, and M. K. Moravvej-Farshi, Designing graphene-based multi-mode acousto-plasmonic devices, J. Lightwave Technol. **37**, 2126 (2019).

[18] F. Taleb, S. Darbari, and A. Khelif, Reconfigurable locally resonant surface acoustic demultiplexing behavior in ZnO-based phononic crystal, J. Appl. Phys. **129**, 024901 (2021).

[19] F. Taleb, S. Darbari, A. Khelif, and H. Taleb, An acoustoelectric-induced tailorable coupled resonator surface acoustic waveguide, J. Phys. D: Appl. Phys. **54**, 225301 (2021).

[20] R. Verba, I. Lisenkov, I. Krivorotov, V. Tiberkevich, and A. Slavin, Nonreciprocal Surface Acoustic Waves in Multilayers with Magnetoelastic and Interfacial Dzyaloshinskii-Moriya Interactions, Phys. Rev. Appl. **9**, 064014 (2018).

[21] H. Zhu and M. Rais-Zadeh, Non-reciprocal acoustic transmission in a GaN delay line using the acoustoelectric effect, IEEE Electron Device Lett. **38**, 802 (2017).

[22] F. Taleb and S. Darbari, Tunable Locally Resonant Surface-Acoustic-Waveguiding Behavior by Acoustoelectric Interaction in ZnO-Based Phononic Crystal, Phys. Rev. Appl. **11**, 024030 (2019).

[23] J. Babaki and F. Nazari, Heterostructure based demultiplexer using solid–solid phononic crystal ring resonators, J. Phys. D: Appl. Phys. **53**, 375301 (2020).

[24] S. E. Zaki, A. Mehaney, H. M. Hassanein, and A. H. Aly, Fano resonance based defected 1D phononic crystal for highly sensitive gas sensing applications, Sci. Rep. **10**, 1 (2020).

[25] M. Sledzinska, B. Graczykowski, J. Maire, E. Chavez-Angel, C. M. Sotomayor-Torres, and F. Alzina, 2D phononic crystals: Progress and prospects in hypersound and thermal transport engineering, Adv. Funct. Mater. **30**, 1904434 (2020).

[26] T.-G. Lee, S.-H. Jo, H. M. Seung, S.-W. Kim, E.-J. Kim, B. D. Youn, S. Nahm, and M. Kim, Enhanced energy transfer and conversion for high performance phononic crystal-assisted elastic wave energy harvesting, Nano Energy **78**, 105226 (2020).

[27] M. Javadi, A. Heidari, and S. Darbari, Realization of enhanced sound-driven CNT-based triboelectric nanogenerator, utilizing sonic array configuration, Curr. Appl. Phys. **18**, 361 (2018).

[28] A. Shakeri, S. Darbari, and M. Moravvej-Farshi, Designing a tunable acoustic resonator based on defect modes, stimulated by selectively biased PZT rods in a 2D phononic crystal, Ultrasonics **92**, 8 (2019).

[29] A. Khelif, Y. Achaoui, S. Benchabane, V. Laude, and B. Aoubiza, Locally resonant surface acoustic wave band gaps in a two-dimensional phononic crystal of pillars on a surface, Phys. Rev. B **81**, 214303 (2010).

[30] Y. Achaoui, A. Khelif, S. Benchabane, L. Robert, and V. Laude, Experimental observation of locally-resonant and bragg band gaps for surface guided waves in a phononic crystal of pillars, Phys. Rev. B **83**, 104201 (2011).

[31] Y. Chen, F. Meng, G. Sun, G. Li, and X. Huang, Topological design of phononic crystals for unidirectional acoustic transmission, J. Sound Vib. **410**, 103 (2017).

[32] X.-F. Li, X. Ni, L. Feng, M.-H. Lu, C. He, and Y.-F. Chen, Tunable Unidirectional Sound Propagation Through a Sonic-Crystal-Based Acoustic Diode, Phys. Rev. Lett. **106**, 084301 (2011).

[33] J.-J. Chen, X. Han, and G.-Y. Li, Asymmetric lamb wave propagation in phononic crystal slabs with graded grating, J. Appl. Phys. **113**, 184506 (2013).

[34] H. Li, W. Liu, T. Yu, T. Wang, and Q. Liao, Simultaneous unidirectional reciprocal filters of electromagnetic and elastic waves based on the modal symmetry of phoxonic crystal waveguides and cavity, Phys. Lett. A **384**, 126499 (2020).

[35] Y. Guo, M. Schubert, and T. Dekorsy, Finite element analysis of surface modes in phononic crystal waveguides, J. Appl. Phys. **119**, 124302 (2016).

[36] F. Gao, A. Bermak, S. Benchabane, M. Raschetti, and A. Khelif, Nonlinear effects in locally resonant nanostrip phononic metasurface at GHz frequencies, Appl. Phys. Lett. **118**, 113502 (2021).